



Modeling and simulation of the effect of scan strategy on spatter movement in laser powder bed fusion

Weihong Cen^{2,3} · Yangzhong Liu² · Honghao Yan² · Zirong Zhou^{1,3} · Zhukun Zhou² · Xin Shang^{1,3} · Shenggui Chen^{2,3} · Yu Long²

Received: 22 June 2022 / Accepted: 8 March 2024 / Published online: 12 April 2024
© The Author(s), under exclusive licence to Springer-Verlag London Ltd., part of Springer Nature 2024

Abstract

The efficiency of LPBF is significantly increased by multi-laser powder layer bed fusion (M-LPBF), which offers multiple application possibilities in the aerospace, biomedical, and industrial industries. However, the spatter phenomenon causes defect formations and contaminations, compromising the processing and thus weakening the quality of the manufactured part. By far, spatters are assumed as fixed particle sizes, or multiple fixed injection angles in existing spatter models, which do not adapt well to the spatter injection from the melt pool. Therefore, a spatter injection model of different particle sizes, initial velocities, and angle ranges is established to simulate gas flow and scanning strategy. In gas–solid coupling simulation, the spatter injection model as discrete phase and N₂ as continuous phase are calculated together. Particle ejection follows the spatter ejection observed by experiments with a high-speed camera. The simulation shows that 300 particles of size 28 μm, 500 particles of size 55 μm, and 1300 particles of size 114 μm are generated, and an average of 63, 116, and 398 particles of the three particle sizes was deposited on the base, respectively. For the three particle sizes, removal rates out of substrate are 79%, 76.8%, and 69.4%, respectively. Besides, under the scanning strategy perpendicular to the gas flow, 114-μm particles are deposited on the start side of the scanning track more than other particles. Most particles are deposited closer to the outlet with counter gas flow. These results will provide an important reference model for M-LPBF and optimize the scanning strategy to reduce the impact of spatters on parts.

Keywords Multi-laser powder bed fusion (M-LPBF) · Gas–solid coupling simulation · Spatter · Scanning strategy

1 Introduction

LPBF is one of the additive manufacturing technologies in which the laser fuses the fine metal powder selectively layer by layer to manufacture parts. M-LPBF is an extension of LPBF that uses multi-lasers for the same task. Owing to its characteristics of manufacturing complex parts, flexibility,

lightweight, and simplicity, it overcomes the limitations of traditional manufacturing methods. It has been widely used in aerospace, biomedical, and other fields [1, 2]. In M-LPBF, there will be fewer but bigger spatters depositing on the printing substrate because the spatter is easier to agglomerate others into a larger spatter when lasers process in overlap areas of the scan strategy. Therefore, it is of significance to develop a spatter model to explore the transport and deposition mechanisms of spatter in the overlapping region of laser processing under different scanning strategies.

Spatter is a by-product of M-LPBF technology and reflection on the state of the melt pool [3]. Three main types of spatters are ejected from the molten pool when the metal powders are melted. Firstly, the metallic spatters are associated with recoil gas pressure and vapor recoil. Secondly, the solid powders are melted, collide and coalesce, referred to as entrainment melting spatters. Thirdly, to reduce the surface tension of the melt pool, the molten metal droplets eject backward to the rear end of the melt pool [4, 5].

✉ Zirong Zhou
hnxtzr@sina.com

✉ Yu Long
longyu@gxu.edu.cn

¹ School of Mechanical Engineering, Dongguan University of Technology, Dongguan 523808, Guangdong, China

² School of Mechanical Engineering, Guangxi University, NanningGuangxi 530000, China

³ Dongguan Institute of Science and Technology Innovation, Dongguan University of Technology, Dongguan 523808, Guangdong, China

Several spatter models based on the spatter spray from the melt pool have been studied in spatter transport and deposition. Wang et al. [6] set up a spatter spray model at 45°, 90°, and 135° angles and the same initial velocity and tracked its trajectory and deposition. They found that 90% of spatters deposited in the chamber are affected by the initial speed of the spatter, injection direction, and laser power. Chen et al. [7] only considered a metal spatter produced by vapor and established a virtual moving model with the spatters vertically jetted. They found no remarkable effect within the range of 60–120° and the denudation zone exposed while the ejection angle was larger than 150°. Anwar et al. [8] used a discrete phase simulation method with normal distribution between 0° and 60° for the backward ejection angle from the collected samples of the earlier experiments in the x – z plane only to track the trajectory of the spatter and plume. They found that the spatters with smaller sizes and masses are more likely to be taken away. Zhang et al. [9] set up a particle ejection model with a backward and forward ejection angle range. The former is estimated to be 127.5° to 165°, while the latter is about 45 to 60°. It was used to study the spatter removal rate influenced by the designed structure of the outlet and inlet of the chamber. As described above, some efforts have done to study spatter removal and its trajectory. However, the spatter ejecting model is not well in line with the spatters spraying from the melt pool because it has the same size particle and initial velocity. Therefore, it is necessary to establish a spatter model based on the initial state of spatter ejection from the melt pool.

Besides, spatter ejection and scanning strategies can affect powder deposition and transfer, resulting in lower forming quality. Anwar et al. [10] believed that the laser scan direction is opposite to gas flow, and spatters will appear on the laser spot input path, reducing the laser energy input. Altmeyen et al. [11] simulated the motion of the spatter source by several layers with in-flow, cross-flow, and counter-flow scan strategies and found that the scanning strategy has a decisive effect on the frequency and intensity of flow separation and particle deposition in the substrate region. Yin et al. [12] studied the interaction between the two-beam laser and materials and observed the change process of the molten pool at its two-laser approaching-meeting-separating motion. They found that the collision of two molten pools would change the flow pattern of the molten pool, resulting in a larger spatter. After years of joint efforts by scholars, spatter deposition under different scan strategies will affect the other processing partition areas in experiments but not in simulations, which has yet to be studied.

Reviewing the published works, the focus on optimization of the spatter ejection angle mainly due to the recoil pressure and vapor becomes obvious. However, little effort has been devoted to modeling the spatter ejection with different sizes in spatter transport and removal following the Marangoni

effect, vapor recoil, and entrainment flow together. In addition, seldom work has efforts to simulate the transport and removal with gas flow influenced by different scan strategies. Therefore, our work includes six different scan strategies to discuss the effects of spatter transport and deposition. Our work focuses on establishing a spatter spray model and investigating the effect of scan strategy on spatter motion and distribution under inert gas flow. Therefore, we studied the effect of the speed, size, and direction of the spatter from the melt pool in spatter spray modeling.

In the article, the research structure is as follows. The nomenclatures are listed in Table 1. Section 2 introduces the fluid and gas–solid simulation theory and establishes the simulation experiment of the spatter model. Section 3 is the experimental scheme for gas flow in the printing chamber, the interactions between gas flow and powder bed, and different scanning strategies. Finally, the spatter spray model is established in our work at Sect. 4 of this article and analyzes the simulation result.

Table 1 Symbol list

Nomenclature	
ρ	Density of the N ₂ gas flow
v	Velocity of the N ₂ gas flow
p	Gas pressure in the chamber
e	Enthalpy
μ	Fluid dynamic viscosity coefficient of N ₂
μ_t	Viscosity coefficient of N ₂ at time t
λ	Thermal conductivity of N ₂
T	Temperature of N ₂
ε	Rate of dissipation of turbulence kinetic energy
G_k	Turbulence kinetic energy with the mean velocity gradient
G_b	Turbulence kinetic energy with the mean velocity gradient and buoyancy
$C_{1\varepsilon}, C_{3\varepsilon}$ C_1, η, σ_k, C_2	Coefficients in ε -equation
S_{ij}	The anisotropy of fluid fluctuating strain rate
S	The mean strain rate of S_{ij}
k	Kinetic energy
x_j	Distance at y -direction
x_i	Distance at x -direction
v_i	Motion speed of particle i
m_i	Mass of particle i
F_{ig}	Gravity of particle i
F_i	Force of friction, gas resistance, collision of particle i
F_{if}	Buoyancy of particle i
F_{id}	Drag force of particle i
I_i	Momentum of inertia of particle i
w	Angular velocity of rotation of particle i
M_{ij}	Torque of particle i

2 Modeling of spatter gas–solid motion

To have a good simplified simulation performance within limited computing power and short simulation time, the following assumptions are introduced in the model. The influence of heat source is neglected, such as evaporation, Marangoni effects, and recoil pressure of multi-physics phenomena. Laser-induced velocity disturbance is slightly above the workbench and less than 1.6 mm at different laser power and can be negligible [6]. The simulation explores the impact of six scan strategies on spatter motion and deposition distribution, focusing on the state of the spatter leaving the melt pool, such as particle size, speed and ejection direction. A virtual moving circular domain mimics the melt pool motion [7, 13]. It makes spatters size, ejection direction, and initial speed from the melt pool a reality as possible and focuses on spatters motion and deposition distribution under the different scan strategies. The simulations are performed with the N₂ and particles inside the printing chamber. The N₂ is regarded as an ideal and incompressible Newtonian fluid. The spatters move in the gas flow, regarded as the calculation of the solid phase. Gas–solid coupling involves the numerical calculation of fluid, solid, and gas–solid coupling. In addition, a simplified model consistent with melt pool spatter spraying is developed in which three different particle sizes are available over three different ranges of velocities and spray angles.

2.1 CFD model

CFD simulations are performed to study spatter motion in the flow field. In order to reduce the computational cost of the simulation process while maintaining acceptable boundary conditions, a Newtonian fluid of nitrogen with constant incompressibility is considered as the ideal fluid inside the printing chamber. In addition, the laser as a heat source melts the powers causing complex multi-physical phenomena. Previously published works simplified the simulation with acceptable accuracy [7, 11, 14]. The heat source is not discussed in this paper, excluding the influence of heat gas turbulence. Philo et al. [15] took some experimental values directly into discrete phase spatter ejection model without heating particles in their research. Wang et al. [6] believed that the laser heat source has little effect on spatters and gas flow velocity after spatters inject out of the melt pool through simulation analysis. Therefore, the initial gas and particle states are considered in this paper. The realizable k-ε turbulent fluid model is used [8, 16, 17]. The dominant equations of the simulation are the fluid continuity model, momentum equation, and energy conservation [9]. The formulas are as follows (1)–(6):

Continuity (mass) equation:

$$\frac{\partial \rho}{\partial t} + \nabla \cdot \rho v = 0 \tag{1}$$

where ρ represents the density of the N₂ gas flow and v represents the velocity of the N₂ gas flow above the formula.

Momentum equation:

$$\rho \frac{\partial v}{\partial t} + \rho \nabla \cdot (v v) = -\rho \nabla p + \rho \mu \nabla^2 v \tag{2}$$

where p represents the fluid pressure and μ represents the fluid dynamic viscosity coefficient.

Energy conservation:

$$\frac{\partial(\rho e)}{\partial t} + \nabla \cdot (\rho e v) = -\nabla \cdot (p v) + \nabla \cdot (\lambda \nabla T) \tag{3}$$

where e represents enthalpy, λ represents thermal conductivity, and T represents temperature.

Transport equation for the turbulence kinetic energy:

$$\frac{\partial}{\partial t}(\rho k) + \frac{\partial}{\partial x_j}(\rho k v_j) = \frac{\partial}{\partial x_j} \left[\left(\mu + \frac{\mu_t}{\sigma_k} \right) \frac{\partial k}{\partial x_j} \right] + G_k + G_b - \rho \epsilon \tag{4}$$

Transport equation for the turbulence dissipation rate ϵ :

$$\frac{\partial}{\partial t}(\rho \epsilon) + \frac{\partial}{\partial x_j}(\rho \epsilon v_j) = \frac{\partial}{\partial x_j} \left[\left(\mu + \frac{\mu_t}{\sigma_k} \right) \frac{\partial \epsilon}{\partial x_j} \right] + \rho C_{1\epsilon} S \epsilon - \rho C_{2\epsilon} \frac{\epsilon^2}{k + \sqrt{v \epsilon}} + C_{1\epsilon} \frac{\epsilon}{k} C_{3\epsilon} G_b \tag{5}$$

where G_k and G_b are generated by the turbulence kinetic energy with the mean velocity gradient and buoyancy, respectively. μ_t is viscosity, and constants $C_{1\epsilon} = 1.44$, $C_{2\epsilon} = 1.9$, $\sigma_k = 1.0$, $C_{3\epsilon}$ is related to the ϵ affected by buoyancy, and C_1 [8] is as follows:

$$C_1 = \max \left[0.43, \frac{\eta}{\eta + 5} \right], \eta = S \frac{k}{\epsilon}, S = \sqrt{2 S_{ij} S_{ij}} \tag{6}$$

2.2 Spatter spray model

When the laser energy is introduced, the powders absorb energy, melt to form a melt pool and generate spatters. To avoid the complex physical fluid flow at the melt pool level and simplify the simulation, some experimental parameters for spatter ejection model establishment were directly adopted from other experimental analysis via high-speed imaging by researchers [6, 15]. The spatter spray model is set up without heating particle but with the initial speed, size and direction of particle. Therefore, it is necessary to do research for experimental values.

Three main types of spatters include droplet spatter, metallic spatter, and powder spatter [18]. However, Young et al. [5] introduced an entrainment melting spatter through

an experiment with a high-speed camera. The powder absorbs energy and vaporizes into metal vapor. Solid spatter was produced through vaporized metal ejecting un-melted powder away from the substrate. Molten powder jets under recoil pressure and forms metallic spatter. Its size is close to the original powder, and its direction is parallel to the opening direction of the depression area of the molten pool [19]. Owing to the Magnani effect, molten metal liquid flows back to the tail of the molten pool, breaks the surface tension, and then transfers into droplet spatter or powder agglomeration particles which are 3–5 times larger than the original particle size. It jets backward to the rear end of the melt pool. The entrainment spatter is the particle surrounding the melt pool driven by the entrainment flow. Some of them are melted by the moving laser to form the melt track or merge with others into bigger ones ejected by the vapor jet with expanding large angle [20, 21].

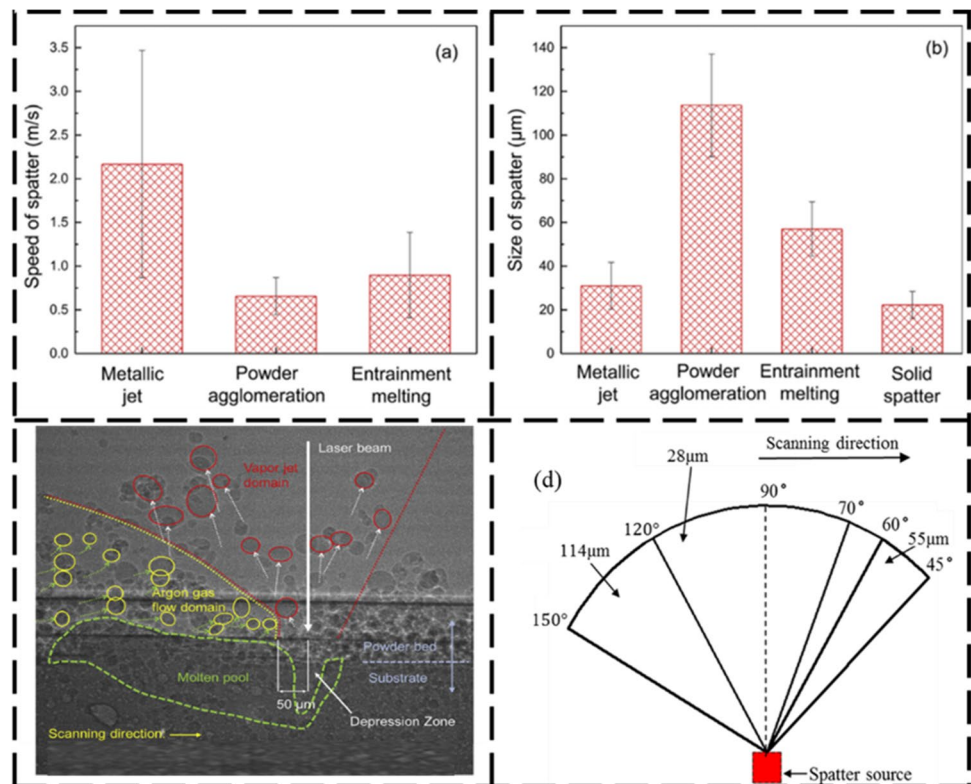
The papers [5, 20] show only when the specific fabrication parameters velocity at 0.4–1.0 m/s and laser power at 340–420 W, the four types of spatter used in our work will appear together and the spraying angles almost meet with the angle ranges set in our model. Many of the parameters used in our study are obtained from reference [5]. The AlSi10Mg distribution of powder sizes is 15–38 μm . The scanning speed is maintained at 1000 m/s. As shown in Fig. 1a, b, spatter sizes and speeds are quantified. A quantified 28 μm of the metallic and solid spatter jet with 2.17 m/s initial speed.

A quantified 114 μm of the powder agglomeration initial jet velocity is 0.66 m/s. A quantified 55 μm of the entrainment melt spatter initial jet velocity is 0.83 m/s. In addition, initial ranges of spatter spray direction can be quantified as 45–150° in the image attained by the high-speed camera in Fig. 1(c). These spout angles are set as 60–90°, 30–60°, and 45–70° for the three spatters, respectively. Finally, the spatters simulation model is established, shown in Fig. 1d. The assumptions of spatter particles in this paper are as follows: (1) three kinds of spatters are set to be spherical; (2) not considering metal vapor effect, Marangoni effects, and recoil pressure; and (3) only considering the diameter, initial velocity, and spray direction of the spatter particles.

2.3 Discrete element method (DEM) model

The spatters generated by the LPBF process settle onto the printing area or the melt tracks, affecting processing quality. Therefore, it is of great significance to track spatter particle trajectory. The protective gas flow affects the spatter tracks by the drag force. The speed of spatter along the direction of the gas flow increases, and the trajectory of spatter becomes longer, which helps with spatter removal. In this article, for tracking its trajectory and spatters distribution, the DEM simulation is carried out to track the motion state and position updating of particles in the fluid domain of the print area. The motion of the particles can be divided into

Fig. 1 Spatters quantified size, speed and direction and model establishment [5], jet direction, and spray model. **a** Spatter speed; **b** spatter size; **c** spatter jet direction [20]; **d** the spatters spray model with three different particle sizes and ejection angle ranges



translation and rotation, which can be calculated with force balance and rotational torque equations of Newton’s second law [10]. The simulation shows the transient simulation force balance of particles, including gravity, the drag force of the airflow, buoyancy, and other possible forces. The force balance equation is as follows:

$$m_i \frac{dv_i}{dt} = F_{ig} + F_{id} + F_{if} + F_i \tag{7}$$

where m_i is the particle mass, v_i is the particle motion speed, F_{ig} is the particle gravity; F_{id} is the particle drag force, F_{if} is the buoyancy of the particle, and F_i represents the force of friction, gas resistance, and collision with a simplified Hertz-Mindlin model.

$$I_i \frac{dw}{dt} = \sum_j M_{ij} \tag{8}$$

where I_i is the moment of inertia of particle, w is the angular velocity of particle rotation, and M_{ij} is the torque of particle.

2.4 CFD-EDEM coupling simulation

Figure 2 shows the main steps in CFD-EDEM, where the blue and pink rectangles represent CFD and EDEM steps [14], respectively, and the flow of data information computation transfers to each other. The initial boundary conditions and coupling simulation are set in the CFD. The SIMPLE algorithm is to calculate fluid state and drag force. According to the established spatter spray model, the EDEM particle factory generates particles with a certain initial speed, size, and direction. The collision forces between particles and between particles and wall are calculated, and then particle torque, speed, and direction of motion are updated after the collision. The information of these particles is transferred to CFD for the next initial

iteration calculation. After updating the gas flow field, it calculates the fluid drag force on the particles and judges whether the iteration time exceeds the preset simulation time. If the iteration time does not exceed the preset iteration time, the next time step will be calculated and determine whether or not the particles are generated. If there are particles generated, the number, size, position, and speed of particles are calculated. If there are no particles generated, the force on the existing particles is calculated directly. If it exceeds the iteration time, the simulation ends.

3 Simulation model setup

3.1 Simulation domain

In the simulation experimental analysis, gas flow is relatively steady and uniform above the substrate with different designs of outlet and inlet [6, 15]. To reduce the computational cost, only the printing base with a 1:1 scale is considered and designed as a fluid domain, and its size is 115 mm × 115 mm in Fig. 3a. Since the maximum height of the spatter particle trajectory is 50–100 mm, a fluid domain is designed, and its size is 115 mm × 115 mm × 200 mm in Fig. 3a.

The simulated fluid is mainly distributed at 1–100 mm above the substrate, and it is uniform [10]. The height of the gas inlet has a great influence on the spatter removal. Therefore, designing a gas inlet rationally is to make the uniform distribution of the fluid domain close to that above the base in the actual chamber. The size of the gas inlet is 20 mm × 115 mm × 15 mm and the size of the gas outlet is 20 mm × 115 mm at a distance of 5 mm above the substrate in Fig. 3a.

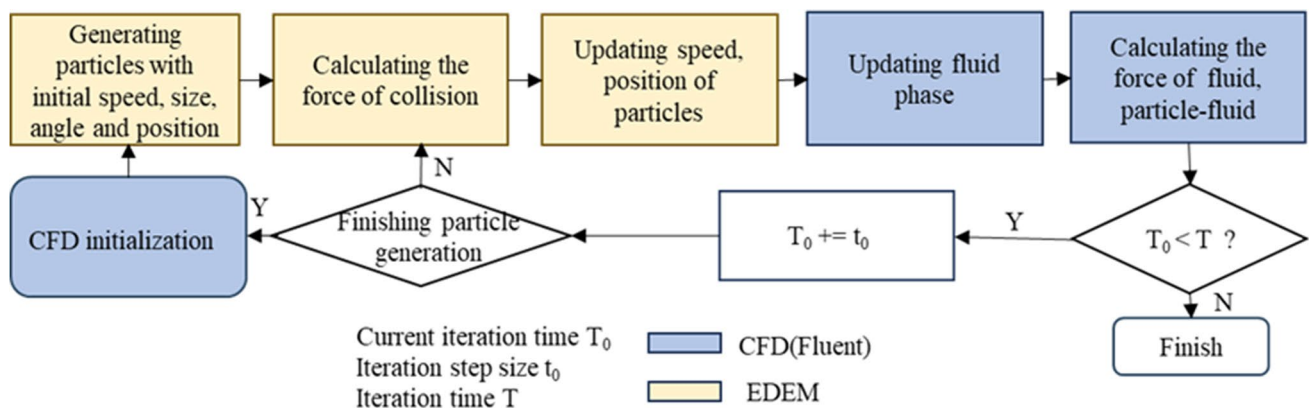
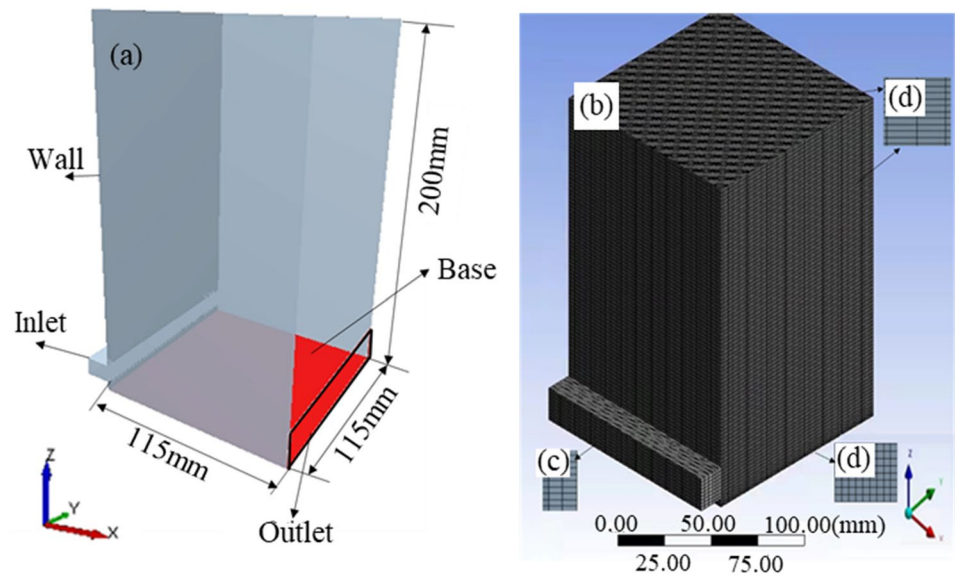


Fig. 2 CFD-EDEM simulation flow chart [14]

Fig. 3 Fluid domain physics model and meshing. **a** Physics model; **b** mesh of the model; **c** the mesh of inlet and outlet; **d** the mesh of wall; **e** the mesh of base



3.2 Meshing

The size of the mesh affects the accuracy of the simulation. To ensure that the simulation result is close to reality and reduce simulation time, the grid size should be rationally designed. In the gas–solid coupling of CFD-EDEM, considering the porosity of particles in the grid, the drag force, and the convergence of the calculation, the grid size is generally above 3–5 times the particle diameter. Therefore, a coarse grid, a medium grid, and a fine grid are used. The sizes of the three grids are 5 mm for the wall, 2.5 mm for the gas outlet and inlet, and 1 mm for the substrate in Fig. 3b–e. There are 1,127,520 mesh nodes and 1,094,340 mesh elements.

3.3 Powder bed setup

Since the diameter of the powder particles reaches the micrometer level, it is easily taken away by the gas flow.

Also, it causes the uneven powder bed in some areas, resulting in poor quality of the molded parts. Therefore, in this paper, we design a 5 mm × 5 mm original powder particle bed to study the interaction between gas flow and powder bed, analyzing the movement of the particles in the powder bed and the changes and states of the fluid.

3.4 Scanning strategy

The scanning strategy influences the trajectory and deposition of the spatter, affecting energy input and processing quality. Therefore, it is necessary to analyze how the spatter moves and where it will deposit. The Phantom V1212 high-speed camera is used to observe spatter motion in a single track. Figure 4 shows that six sets of scan strategies are set for the virtual “melt pool” movement. Each scan strategy has 20 tracks with a hatch of 50 μm, and the length of one track is 10 mm.

Fig. 4 Scan strategy diagram. **a** Printing area in the base; **b** perpendicular to gas flow; **c** perpendicular and opposite to the flow; **d** parallel and opposite to the flow; **e** 45° to gas flow; **f** 135° to gas flow; **g** perpendicular to gas flow and the bilateral scan direction

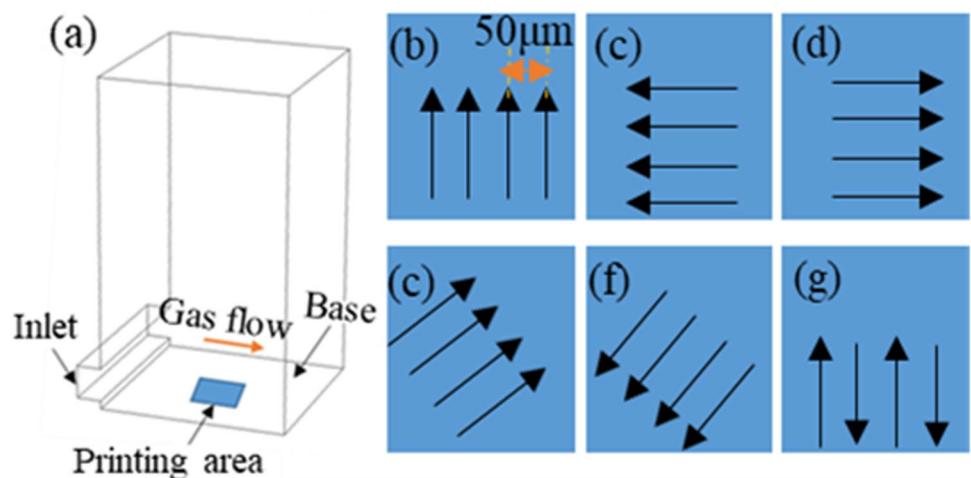


Table 2 Simulation parameters

Name	Property	Unit	Value/method
N ₂	Density	kg/m ³	1.138
	Dynamic viscosity	Pa•s	1.663e−05
Velocity-inlet	Velocity	m/s	3.0
Outflow	Flow rate weighting	–	1
Fluid viscosity model	<i>k</i> -epsilon	–	Realizable
Drag model	Drag law	–	Spherical

Table 3 Different collision coefficients [5]

Collision property	Particle–particle	Particle–base/wall
Coefficient of restitution	0.5	0.01
Coefficient of static friction	0.75	100
Coefficient of rolling friction	0.01	0.01

Table 4 The types and properties of the material

Spatter particle property	316 L	AlSi10Mg
Poisson ratio	0.3	0.3
Bulk density (kg/m ³)	7850	2670
Young’s modulus (MPa)	2200	–
Shear modulus (MPa)	–	8 × 10 ⁴

3.5 Simulation parameter and boundary conditions

The data information of the simulations needs to be transferred to each other in real time to calculate the particle motion state correctly. Therefore, the time is set to be

transient in Fluent. The realizable *k*-epsilon model is selected. The gas flow inlet is the velocity inlet, and its speed is 3 m/s. The gas flow outlet is the flow outlet. The gas flow turbulent intensity is 5%, and the gas flow turbulent viscosity coefficient is 10. The gas–solid coupling is a two-phase flow coupling. Eulerian multi-phase flow simulation is selected. The fluid is nitrogen (N₂), and the discrete phase is the solid particles. The default drag model of the fluid is used. All fluid domains are initialized and computed using the SIMPLE solver. Other simulation parameters are shown in Tables 2, 3, and 4.

4 Results and discussion

4.1 Uniformity analysis of gas flow inertia

In Fig. 5a, the velocity cloud map in the fluid domain is stable at the Y–Z plane 57.5 mm from the side wall, the X–Z plane 72.5 mm from the inlet, and the X–Y plane 15 mm above the base. The Y–Z plane shows that the velocity is mainly the same height as the gas flow inlet, and its range is 2.7–3.18 m/s (Fig. 5b), reaching the expected velocity value. Gas velocity, a little above the substrate, is relatively low, so the powder particles are not easily taken away. The X–Z plane shows that there will be a tiny eddy fluctuating gas flow, but its height is low, and it can be ignored (Fig. 5c). The X–Y plane cloud map shows the uniformity of the velocity and gas flow (Fig. 5d). Behind the inlet, the velocity will decrease slightly at 20–58 mm and then become stable. However, the overall fluid velocity uniformity performs well, which plays an essential role in removing spatter particles. It is conducive to the settlement area farther away from the printing area, which is beneficial to improving the quality of the parts.

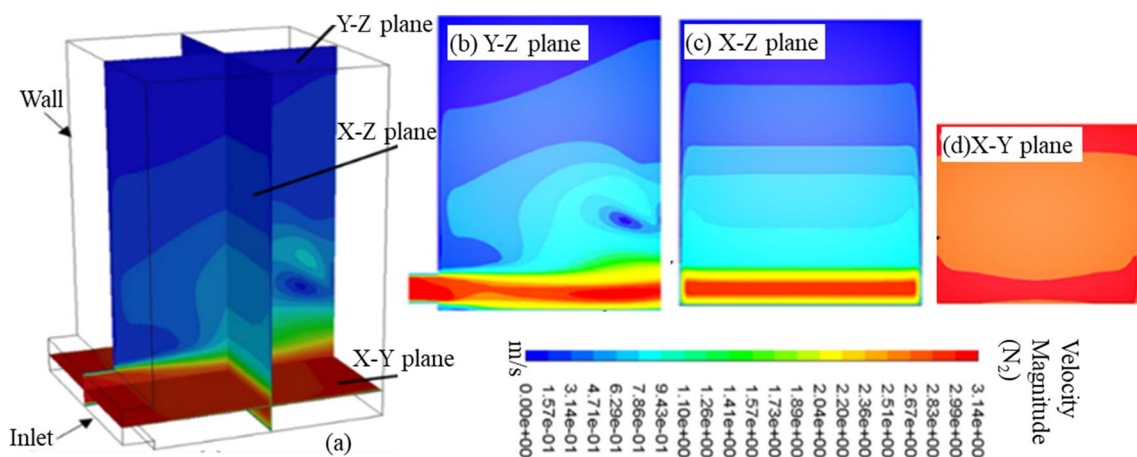


Fig. 5 The velocity of N₂ distribution. **a** The velocity contour in three different planes; **b** Y–Z plane; **c** X–Z plane; **d** X–Y plane

4.2 Motion analysis of particles on the powder bed surface

In Fig. 6a, there are 27,472 powder particles distributed in the area of $5\text{ mm} \times 5\text{ mm}$, and the filling rate of powder at the first layer reaches 68.68%. After simulation, it finds that the powder particles on the substrate affect the gas flow speed and direction, shown in Fig. 6b. The uniformity of gas is relatively disordered, but the gas flow speed becomes low. However, in the region higher than 1 mm, the flow field changes slightly. Particles are generally generated at a relatively high initial velocity, and the impact of flow field change on the spatter particle trajectory can be ignored. As shown in Fig. 6c, with a gas speed of 3 m/s, most powder particles have no change in speed, but only a small number of powder particles have a low speed. That is because the particles generated following a Gaussian distribution, and the smaller ones overcome the friction and slip slowly.

4.3 Validation of the spatter particle ejection model

The spray model with the three kinds of spatter particles in this experiment is established at different initial spray angle ranges and speeds. The spray model moves along the scanning direction in 1 m/s without gas flow, and the simulation results are shown in Fig. 7a. It shows that the three kinds of spatters still eject backward to the scanning direction, and most of the spray angle is about $105\text{--}135^\circ$ relative to the scanning direction. This is similar to the results observed by the high-speed camera in the article of Young et al. [5] as shown in Fig. 7b. In addition, Yin et al. [22] and Wang et al. [23] uncovered the same phenomenon in experimental analysis. Therefore, the established spatter particle model is used as one of the primary conditions of the simulation experiment. Spatters motion is opposite to the scan direction and then the same as gas flow with the effect of the gas flow

in Fig. 7c, d. In Fig. 7c, rare particles in $28\text{ }\mu\text{m}$ are deposited on the substrate and have an average longest distance from the melt pool. While most $114\text{-}\mu\text{m}$ particles are deposited closer to the printing areas and have an average shortest distance relative to another two particles. For the second place, the $55\text{-}\mu\text{m}$ particles are deposited on the substrate and have a flight distance. It shows that the larger the particle mass and the larger the particle ejection angle relative to the scanning direction, the shorter the flight distance it has. Larger particles are more likely to deposit on the substrate area than smaller ones.

The spatter motion by scanning strategy simulation results of the tracks with 45° to gas flow is compared with the images obtained by the high-speed camera presented in Fig. 8. Within the parameter window suitable for manufacturing, the trend of spatters spraying is almost the same. The two papers show the same result that the initial trajectory of spatters is parallel to the scanning track and then aligns to the direction of the gas flow under the gas flow drag force. The result agrees with that of Schwerz et al. [24] as well as Bidare et al. [25], even though the materials are completely different in three different experiments. In addition, the spatters move to both sides of the scan track in Fig. 8c, consistent with its spraying out of the melt pool observed under the high-speed camera in Fig. 8d. The momentum of the spatter interacts with the gas flow; therefore, it is difficult for the gas flow to remove spatters partly ejecting to $+Y$ than $-Y$. Therefore, the gas flow plays an impact on the spatter redistribution.

4.4 Spatter deposition and removal study for six different scanning strategies

As shown in Fig. 9, scanning areas are divided into six partitions to study the effect on spatters deposition distribution on the substrate. After simulation, most $55\text{-}\mu\text{m}$ particles of

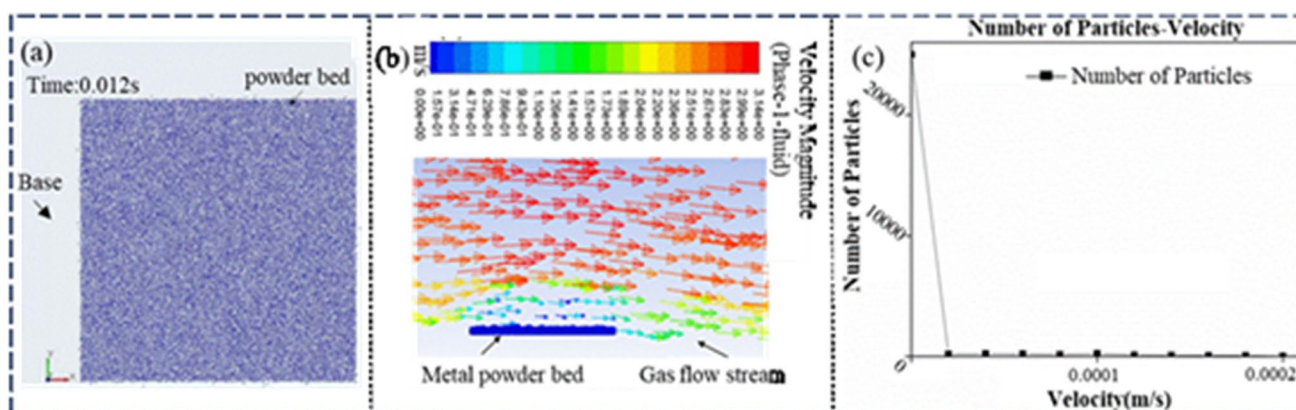


Fig. 6 The velocity change of metal powder bed and gas flow. **a** Metal powder bed; **b** the velocity of gas flow above powder bed; **c** the histogram of different velocities of particles

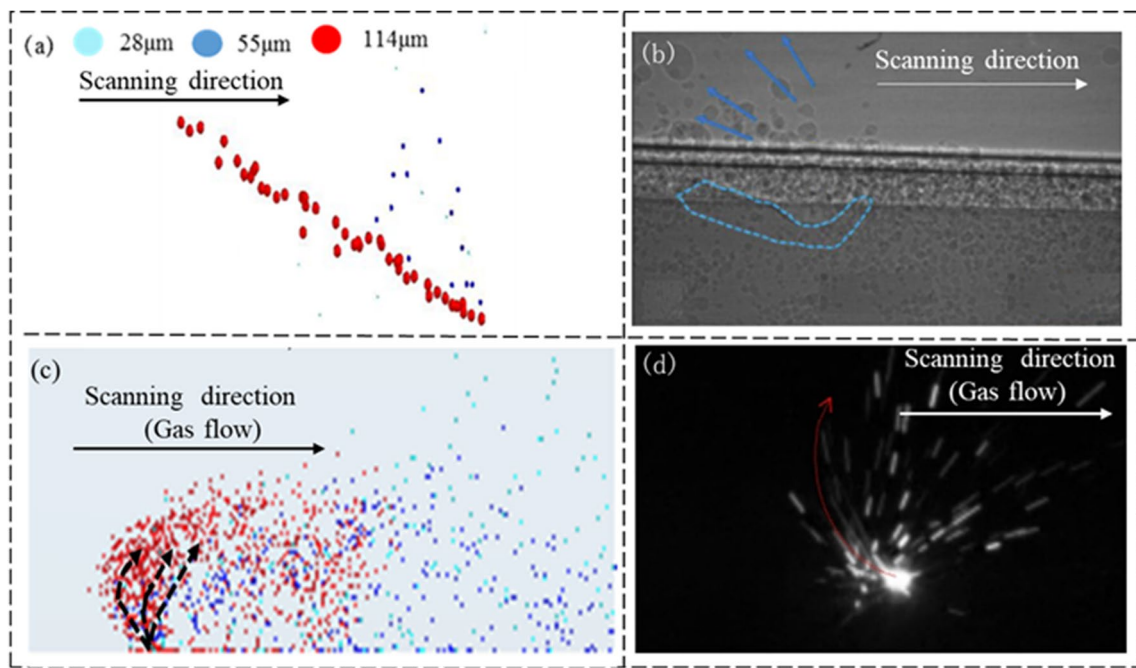
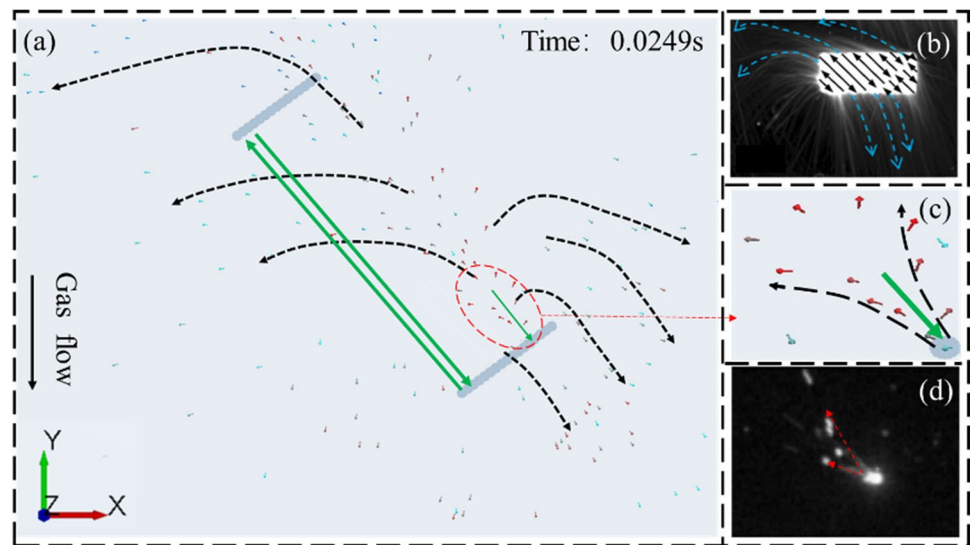


Fig. 7 Spatter motion simulation and spatter single line with a high-speed camera. **a** Spatter motion in a single track; **b** spatter motion under a high-speed camera [5]; **c** spatter movement with gas flow; **d** spatter movement with gas flow high-speed camera

Fig. 8 Spatter motion with 45° to gas flow scanning strategy. **a** Spatter simulation; **b** spatter motion under a high-speed camera [24]; **c** spatter movement in the track; **d** spatter movement in the track under the high-speed camera



entrainment melting spatters are deposited near the scanning area, and they are hard to be removed. That is because they are produced with a lower speed, smaller spray forward angle, and larger size by recoil steam entrainment and easier to collide with other particles causing deposits close to the printing areas. Figure 9a shows that most spatters deposit on one side of the printing areas after the simulation of scanning direction at 90° to gas flow. Especially, 114-µm spatter jet direction along the tail of molten pool deposit mainly at the beginning of scanning lines. Spatters deposit closer

to the outlet by the scan strategy of the scanning direction opposite to the gas flow in Fig. 9b than that along the gas flow in Fig. 9c. The reasons are that most particles in 114 µm eject backward to the tail of the scanning direction, and the speed of spatters will become lower until stopping and then go up along the gas flow with the effect of gas flow. Therefore, spatters with initial velocity against the gas flow are close to the printing area and more likely to move to the laser input path, affecting powder melting. A good spatter deposition distribution by the scan strategy parallel to the

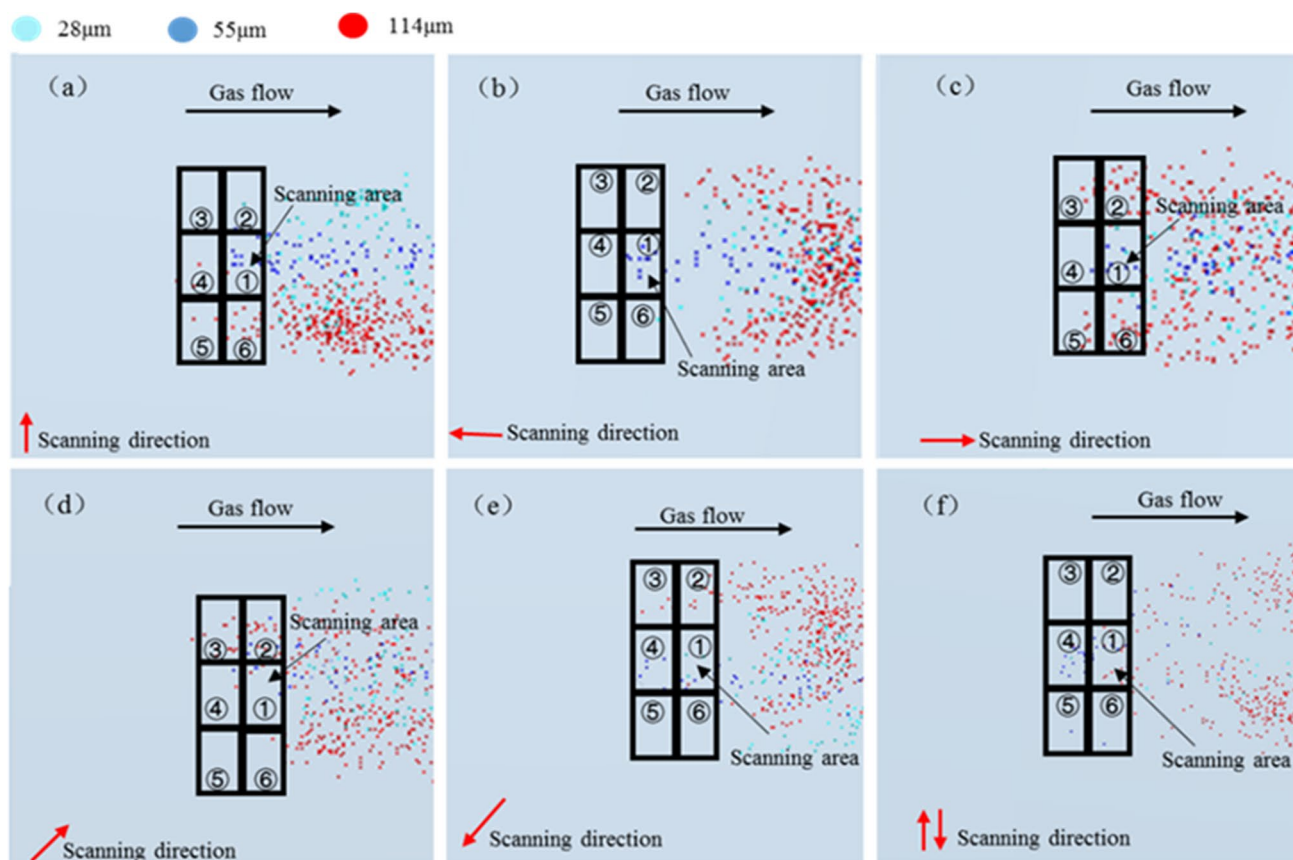


Fig. 9 Spatter deposition in different scan strategy. **a** Perpendicular to gas flow; **b** parallel and opposite to the flow; **c** parallel and along to gas flow; **d** 45° to gas flow; **e** 135° to gas flow; **f** perpendicular to gas flow and the bilateral scan direction

gas flow will occur, and spatters deposit more on the second, third, fifth and sixth scanning areas than the first and fourth areas in Fig. 9c. That is because the spatter sprays and scatters on both sides of the scan line, and the component vector velocity of particles is opposite to gas flow. It finds that more spatters deposit close to the scan area compared with the results in Fig. 9b, and the component vector velocity of particles on one side is consistent with the direction of gas flow. In contrast, the one on another is in the opposite direction. Therefore, particles have different trajectories and deposition distances from the melt pool on both sides of the track. It conforms to what Scherz et al. [24] observed with a high-speed camera. Within the parameter window suitable for manufacturing, the trend of spatters spraying is almost the same. The two papers show the same result that the initial trajectory of spatters is parallel to the scanning track and then aligns to the direction of the gas flow under the gas flow drag force. The result agrees with Scherz et al. [24] as well as Bidare et al. [25], even though the materials are completely different in three different experiments. Besides, spatters are closer to the outlet in Fig. 9e than those in Fig. 9d. Most particles in 114 µm eject backward to the tail of the scanning direction and spatter component vector

velocity along and in line with the gas flow in Fig. 9e. As shown in Fig. 9f, particles are more evenly distributed on both sides of the scan area by the tracks of scan strategy with dual scan direction and at 90° to the gas flow than those shown in Fig. 9a. Therefore, the scanning strategy with the bidirectional tracks opposite to gas flow is adapted to avoid the spatters agglomeration and uneven parts processing quality on the region where the beginning of tracks is located. Spatters have good deposition distribution on the substrate and longer trajectory and deposit close to the outlet.

With the influence of the gas flow, most of the particles are deposited outside the printing area. The removal rate is the proportion of each type of particle removed from the base relative to the total amount generated for each type. For the 28-µm, 55-µm, and 114-µm particles, they have been deposited on the printing area with an average number of 63, 116, and 398. Their removal rates are 79%, 76.8%, and 69.4%, respectively, as shown in Fig. 10. It can be attributed that small particles of size 28 µm have a higher vertical rise and removal rate owing to initial high speeds and low quality. Besides, 28-µm particles have a longer fly trajectory, which deposits less on the base and more outside the base, as shown in Fig. 7c. Because of heavier masses, lower

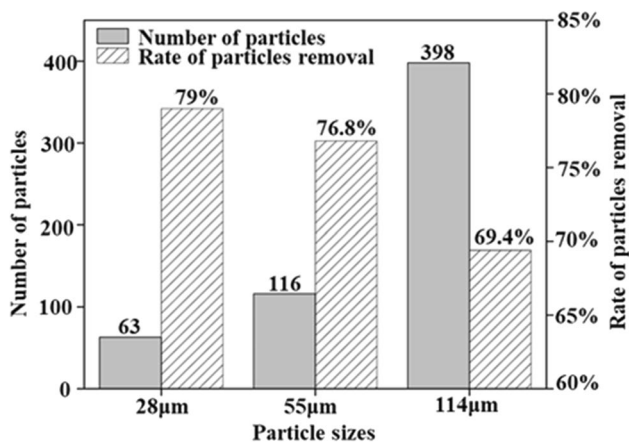


Fig. 10 Number of particles in the base and removal rate out of the base

initial speeds, and shorter fly trajectories, the 55-µm and 114-µm particles are not enough taken away by the protective gas flow in Fig. 7c. Therefore, 28-µm particles have a higher removal rate. It can be concluded that the particles with small sizes and large spray angles are easier to be taken away by the gas flow, indicating that the particle fusing with others into a large particle is more difficult to be removed.

5 Conclusion

Since deposition and removal of spatters have a significant impact on processing in LPBF. In this paper, according to the spatters ejecting from the molten pool, a new spatter model with 28 µm, 55 µm, and 114 µm of three particle sizes and different initial jet speeds and angle ranges of 45–70°, 60–120°, and 120–150° is established. In addition, spatter deposition and removal rate are analyzed under six different scanning strategies within the gas–solid simulation. From the results presented and discussions in this paper, we reach the following conclusions: During the spatter motion simulations, the spatter particles eject backward relative to the single-track scanning direction, and the height of the spatter particle in 28 µm is the highest, which is consistent with the observation of spatter under the high-speed camera and in line with the spatters ejecting from the melt pool.

1. At a suitable gas velocity, a slight velocity variation between the gas flow and the powder bed is shown after simulation. Therefore, the velocity effect between the gas flow and the powder bed can be negligible.
2. Compared with spatter simulation under six different scanning strategies in our work, the spatter particle of size 114 µm is closer to the outlet under the scan strategy

of parallel and opposite to the gas flow. Most spatters deposit on both sides of the scan area when the tracks of the scan strategy are parallel to the gas flow. Most spatters deposit on one side of the scan areas when the tracks of scan strategy are perpendicular to gas flow, which is not conducive to fully melting powders by laser in the next layer. Moreover, spatters are better distributed when the bidirectional tracks in the scan strategy are perpendicular to gas flow. In the scan strategy of 45° or 135° to gas flow simulation, one side of the scan area has more spatters than another one. The poor distribution of spatters affects the forming quality in the next laser, even the whole part.

3. It is easier to remove particles of size 28 µm with a large initial velocity and large spray angle by gas flow, while particles of size 114 µm are relatively more difficult. The removal rates for particles of size 28 µm, particles of size 55 µm, and particles in 114 µm are 79%, 76.8%, and 69.4%, respectively. Therefore, the smaller the particle it is, the easier it is to remove.

Finally, the spatter particles are only considered as the solid state, not the gaseous and liquid states. Particles cannot be merged with other particles when colliding and cannot reflect the actual well. Simulations are only in one partition. Spatter interference between multiple regions needs to be better studied when processing. The next step is to study the gas–liquid–solid spatter ejection model and the interaction of multi-region spatters for M-LPBF.

Author contribution Weihong Cen: conceptualization, investigation, methodology, simulation, data curation, original draft, and writing. Yangzhong Liu: simulation and data curation. Honghao Yan: data curation and revising the draft. Zirong Zhou: resources and supervision. Zhukun Zhou: instruction for simulation. Xin Shang: revising draft. Shenggui Chen: resources and supervision. Yu Long: fund acquisition, conceptualization, revising draft, and supervision.

Funding This work is financially supported by the Key-Area Research and Development Program of Guangdong Province (Grant No. 2020B090924002), Guangdong Province Basic and Applied Basic Research Major Project (Grant No. 202019071810200001), Dongguan Sci-tech Commissioner (Grant No. 20211800500102), the National Key R&D Program of China (Grant No. 2021YFE0203500), and the Special Funds for Local Scientific and Technological Development guided by the Central Government (Grant No. GKZY21195029).

Data availability The data generated and analyzed are included and properly cited in this article.

Code availability Not applicable.

Declarations

Ethics approval Not applicable.

Consent to participate Not applicable.

Consent for publication All authors have read and agreed to the published version of the manuscript.

Conflict of interest The authors declare no competing interests.

References

- Englert L, Czink S, Dietrich S, Schulze V (2022) How defects depend on geometry and scanning strategy in additively manufactured AlSi10Mg. *J Mater Process Technol* 299:117331. <https://doi.org/10.1016/j.jmatprotec.20-21.117331>
- Du RE, Chung SG, Jin MJ, Cho JW (2021) Melt pool oxidation and reduction in powder bed fusion. *Addit Manuf* 41:101982. <https://doi.org/10.1016/j.addma.20-21.101982>
- Repossini G, Laguzza V, Grasso M, Colosimo BM (2017) On the use of spatter signature for in-situ monitoring of laser powder bed fusion. *Addit Manuf* 16:35–48. <https://doi.org/10.1016/j.addma.20-17.05.004>
- Gunenthiram V, Peyre P, Schneider M, Dal M, Coste F, Fabbro R (2017) Experimental analysis of spatter generation and melt-pool behavior during the powder bed laser beam melting process. *J Mater Process Technol* 251:376–386. <https://doi.org/10.1016/j.jmatprotec.2017.08.012>
- Young ZA, Guo Q, Parab ND, Zhao C, Chen L (2020) Types of spatter and their features and formation mechanisms in laser powder bed fusion additive manufacturing process. *Addit Manuf* 36:101438. <https://doi.org/10.1016/j.addma.20-20.101438>
- Wang J, Zhu Y, Li H, Liu S, Wen S (2021) Numerical study of the flow field and spatter particles in laser-based powder bed fusion manufacturing. *Int J Precision Eng Manuf-Green Technol*: 1–12. <https://doi.org/10.1007/s40684-021-00357-0>
- Chen H, Yan W (2020) Spattering and denudation in laser powder bed fusion process: multiphase flow modelling. *Acta Mater* 196:154–167. <https://doi.org/10.1016/j.actamat.2020.06.033>
- Anwar AB, Ibrahim IH, Pham QC (2019) Spatter transport by inert gas flow in selective laser melting: a simulation study. *Powder Technol* 352:103–116. <https://doi.org/10.1016/j.powtec.20-19.04.044>
- Zhang X, Cheng B, Tuffile C (2020) Simulation study of the spatter removal process and optimization design of gas flow system in laser powder bed fusion. *Addit Manuf* 32:101049. <https://doi.org/10.1016/j.addma.2020.101049>
- Anwar AB, Pham QC (2017) Selective laser melting of AlSi10Mg: effects of scan direction, part placement and inert gas flow velocity on tensile strength. *J Mater Process Technol* 240:388–396. <https://doi.org/10.1016/j.jmatprotec.2016.10.015>
- Altmeppen J, Nekić R, Wagenblast P, Staudacher S (2021) Transient simulation of particle transport and deposition in the laser powder bed fusion process: a new approach to model particle and heat ejection from the melt pool. *Addit Manuf* 46:102135. <https://doi.org/10.1016/j.addma.2021.102135>
- Yin J, Wang D, Wei H, Yang L, Ke L, Hu M, Xiong W, Wang GQ, Zhu HH, Zeng X (2021) Dual-beam laser-matter interaction at overlap region during multi-laser powder bed fusion manufacturing. *Addit Manuf* 46:102178. <https://doi.org/10.1016/j.addma.2021.102178>
- Li X, Tan W, Asme M (2021) Numerical modeling of powder gas interaction relative to laser powder bed fusion process. *J Manuf Sci Eng* 143:1–7. <https://doi.org/10.1115/1.404>
- Chien CY, Le TN, Lin ZH, Lo YL (2021) Numerical and experimental investigation into gas flow field and spattering phenomena in laser powder bed fusion processing of Inconel 718. *Mater Des* 210(8):110107. <https://doi.org/10.1016/j.matdes.2021.110107>
- Philo AM, Sutcliffe CJ, Sillars S, Siens J, Brown SGR, Lavery NP (2020) A study into the effects of gas flow inlet design of the Renishaw AM250 laser powder bed fusion machine using computational modelling. *Solid Freeform Fabrication 2017: Proceedings of the 28th Annual International Solid Freeform Fabrication Symposium-An Additive Manufacturing Conference, SFF 2017*, 1203–1219
- Shih T-H, Liou WW, Shabbir A, Yang Z, Zhu J (1995) A new $k\text{-}\mu$ eddy viscosity model for high Reynolds number turbulent flows. *Comput Fluids* 24(3):227–238. [https://doi.org/10.1016/0045-7930\(94\)00032-T](https://doi.org/10.1016/0045-7930(94)00032-T)
- Kim SE, Choudhury D, Patel B (1999) Computations of complex turbulent flows using the commercial code fluent. *Model Complex Turbulent Flows Springer* 7:259–276. https://doi.org/10.1007/978-94-011-4724-8_15
- Wang D, Wu S, Fu F, Mai S, Yang Y, Liu Y, Song C (2017) Mechanisms and characteristics of spatter generation in slm processing and its effect on the properties. *Mater Des* 117:121–130. <https://doi.org/10.1016/j.matdes.2016.12.060>
- Wu Z, Xu Z, Fan W (2022) Online detection of powder spatters in the additive manufacturing process. *Measurement* 194:111040. <https://doi.org/10.1016/j.measurement.2022.111040>
- Guo Q, Zhao C, Escano LI, Young Z, Xiong L, Fezzaa K, Chen L (2018) Transient dynamics of powder spattering in laser powder bed fusion additive manufacturing process revealed by in-situ high-speed high-energy x-ray imaging. *Acta Mater* 151:169–180. <https://doi.org/10.1016/j.actamat.2018.03.036>
- Li X, Zhao C, Sun T, Tan W (2020) Revealing transient powder-gas interaction in laser powder bed fusion process through multi-physics modeling and high-speed synchrotron x-ray imaging. *Addit Manuf* 35:101362. <https://doi.org/10.1016/j.addma.2020.101362>
- Yin J, Yang L, Yang X, Zhu H, Wang D, Ke L, Wang Z, Wang G, Zeng X (2019) High-power laser-matter interaction during laser powder bed fusion. *Addit Manuf* 29:100778. <https://doi.org/10.1016/j.addma.2019.100778>
- Wang D, Dou W, Ou Y, Yang Y, Tan C, Zhang Y (2021) Characteristics of droplet spatter behavior and process-correlated mapping model in laser powder bed fusion. *J Market Res* 12:1051–1064. <https://doi.org/10.1016/j.jmrt.2021.02.043>
- Schwerz C, Raza A, Lei X, Nyborg L, Hryha E, Wirdelius H (2021) In-situ detection of redeposited spatter and its influence on the formation of internal flaws in laser powder bed fusion. *Addit Manuf* 47:102370. <https://doi.org/10.1016/j.addma.20-21.102370>
- Bidare P, Bitharas I, Ward RM, Attallah MM, Moore AJ (2018) Fluid and particle dynamics in laser powder bed fusion. *Acta Mater* 142:107–120. <https://doi.org/10.1016/j.actamat.2017>

Publisher's Note Springer Nature remains neutral with regard to jurisdictional claims in published maps and institutional affiliations.

Springer Nature or its licensor (e.g. a society or other partner) holds exclusive rights to this article under a publishing agreement with the author(s) or other rightsholder(s); author self-archiving of the accepted manuscript version of this article is solely governed by the terms of such publishing agreement and applicable law.